Since the mid-1980s, a number of researchers have developed computer-aided diagnostic (CAD) schemes for detection and classification of various kinds of abnormalities such as microcalcifications and masses in mammograms,[4,5] pulmonary nodules and diffuse lung diseases in CT,[6–8] and colonic polyps in CT colonography.[9,10] Besides, the clinical usefulness of CAD schemes has been studied.[11] In the detection of intracranial aneurysms by MRA, CAD schemes would be useful in assisting radiologists. Therefore, we developed a computerized scheme for automated detection of unruptured intracranial aneurysms in MRA based on the use of a three-dimensional (3-D) selective enhancement filter for dots (aneurysms).[12,13] Twenty-nine cases with 36 unruptured aneurysms (diameter: 3–26 mm, mean of 6.6 mm) and 31 nonaneurysm cases were tested. The CAD scheme correctly detected all of 36 aneurysms with 2.4 false positives per patient based on a leave-one-out-by-patient test method. However, for a large database (53 cases with 61 aneurysms and 62 nonaneurysm cases), the previous scheme[12] above produced 5.8 false positives per patient at a sensitivity of 97%. As a result of investigation on the false positives, we found that about 65% of the false positives were of the single-vessel type and the bifurcation type. Therefore, in this study, we focused on removing these two types of false positives.

Our purpose of this study was to improve the CAD scheme for the automated detection of unruptured intracranial aneurysms in MRA by use of image features of small protrusions extracted based on a shape-based difference image (SBDI) technique. The SBDI technique was based on the shape-based difference between an original segmented vessel and a vessel with suppressed local changes in thickness. The performance of our CAD scheme was evaluated by the use of 115 cases (53 cases with 61 aneurysms and 62 nonaneurysm cases) based on a free-response receiver operating characteristic (FROC) curve. For an estimation of the robustness of our scheme, we tested it for an independent set of 63 cases (34 cases with 36 aneurysms and 29 nonaneurysm cases) acquired from a different MRI at a different institution.

II. METHODS AND MATERIALS

A. Overall scheme

Figure 1 shows the overall scheme developed in this study, where a feature extraction procedure based on the SBDI technique was incorporated into the previous scheme.[12] Our approach for the identification of initial candidates was based not only on enhancement of aneurysms by use of a selective enhancement filter for dots (aneurysms),[14] but also on finding short branches on parent skeletons in skeleton images, which can indicate the high likelihoods of small aneurysms.[12] The image features of aneurysm candidates were determined based on candidate regions segmented by the use of a region growing technique. In addition to these features, in this study, useful image features related to small protrusions were extracted from the SBD regions (obtained by the SBDI technique), which could be small aneurysms for true positives, but thin or very small regions for false positives. Finally, false positives were removed by use of rule-based schemes and linear discriminant analysis (LDA).

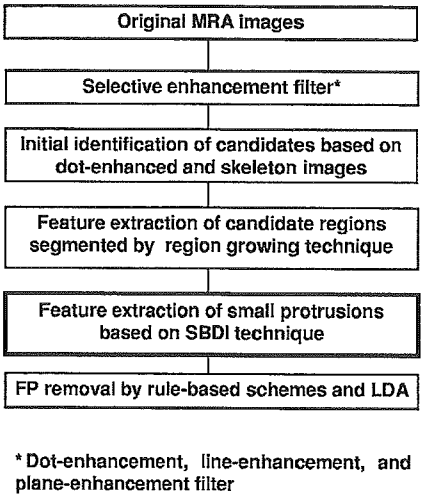

FIG. 1. Overall CAD scheme for detection of intracranial aneurysms at 3-D MRA.

B. Initial identification of aneurysm candidates based on dot-enhanced image and skeleton image

The selective enhancement filters for dots,[14] which can enhance dot-like objects, were applied to isotropic 3-D MRA images. Figure 2 shows an original MRA image with a large aneurysm within a search region, and its dot-enhanced image, where the aneurysm was enhanced well. For avoiding picking up a number of regions irrelevant to vessels, the search region was determined for identifying initial candidates by dilation of major vessels segmented in an MRA image.[15] The initial candidates were identified with a multiple-gray-level thresholding technique for finding local peaks of voxel values in 3-D dot-enhanced images within the search region, and the candidate regions were segmented by the use of a region growing technique.[12] However, some

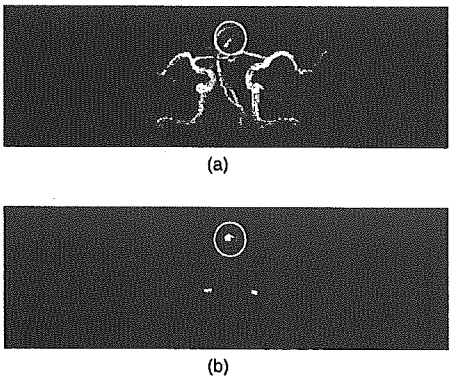

FIG. 2. An illustration of (a) an original MRA image and (b) its corresponding dot-enhanced image, all of which were produced by MIP image processing. Circles indicate a large aneurysm with a diameter of 10.0 mm on the top of the basilar artery.

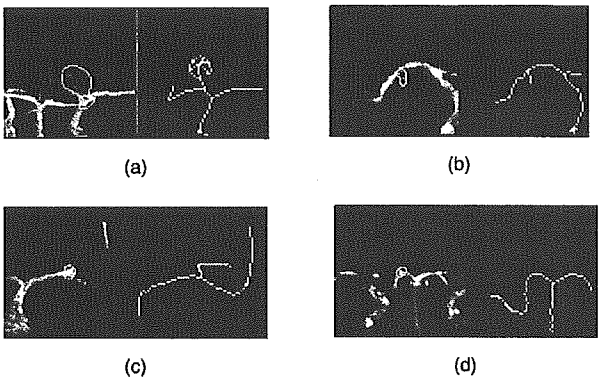

FIG. 3. Illustration of four types of aneurysms in original images with segmented regions (white lines) and the corresponding skeleton images. (a) Large type, (b) short-branch type, (c) bifurcation type, and (d) single-vessel type.

small aneurysms adjacent to a bending region of a thick vessel were not enhanced well by the dot enhancement filter, because the bending region was strongly enhanced. In that case, the bending region was picked up as an "aneurysm" candidate instead of the true aneurysm. However, we found that such small aneurysms became a short branch on the parent vessel in the skeleton image. Therefore, if the short branch was detected in a spherical area adjacent to the original candidate region (e.g., bending region) in a skeleton image, the short branch was considered to be an additional candidate of the short branch type and was segmented based on a region-growing technique.

C. Feature extraction of candidate regions segmented by a region growing technique

Image features of candidates were determined based on the regions segmented by use of a region growing technique in the dot-enhanced images and original images. Our segmentation method was based on finding a large change in some image features, which implied that the candidate region merged with its adjacent background or other candidates, as the candidate region grew.[12] All candidates were classified into four categories based on the effective diameter and local structures determined from the skeleton image, i.e., large type, short-branch type, bifurcation type, and single-vessel type, as shown in Fig. 3, because the image features of aneurysms and false positives in each category differed from each other. Short-branch-type candidates were segmented based on region growing in the original image from the short branch as a seed region. For segmented regions of aneurysm candidates, gray-level features and morphological features as shown in Table I were determined in the original images, dot-enhanced images, line-enhanced images, plane-enhanced images, distance-transformed images, and skeleton images; the definitions of image features are described in the Appendix.

For large aneurysm candidates, image features relevant to the characteristics of large aneurysms were determined, i.e., the average voxel value and the standard deviation (SD) of the voxel value in the core and rind regions of the segmented candidates in the original images, because the characteristics of the large aneurysms were different from those of small aneurysms.[12] In addition, specific features for the short-branch-type candidates were determined, i.e., the protrusion length and the average distance value in the candidate region obtained from the distance-transformed image.

D. Shape-based difference image (SBDI) technique

The SBDI technique was developed for the extraction of local changes in vessel thickness based on distance-transformed images and skeleton images. The local changes in the thickness could be caused by aneurysms, stenosis, etc. The overall algorithm of the SBDI technique is shown in Fig. 4. A vessel with a candidate was segmented within a volume of interest by use of a segmentation method (e.g., a region growing technique as used in this study). The SBDI technique is based on the shape-based difference (SBD region) between an original segmented vessel and a vessel with suppressed local change in thickness by use of logical Exclusive OR (XOR) operation. In this study, SBD regions were ex-

TABLE I. Gray-level features and morphological features used in this study.

Gray level features:
Average voxel value
Standard deviation (SD) of voxel value
Relative contrast to average voxel value
Relative difference is SD of voxel values between inside and outside regions
Relative difference in average voxel values between inside and outside regions
Morphological features:
Effective diameter
Sphericity
Relative SD of the distance between centroid and surface
Maximum and minimum distance between centroid and surface
Difference between maximum and minimum distance betweeen centroid and surface
Maximum or average distance value of distance-transformed image
Relative difference in maximum distance between inside and outside regions
Length of protrusion

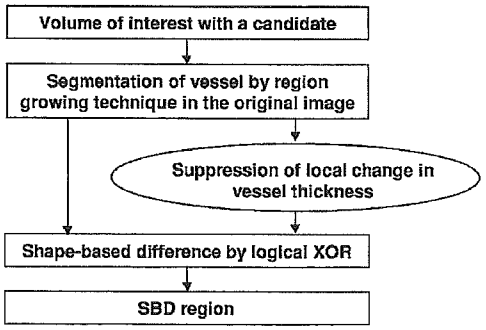

FIG. 4. Overall algorithm of a shape-based difference image (SBDI) technique.

tracted as "small protrusions" or "small aneurysms" from parent vessels, and SBD image features were calculated.

Figure 5 shows the algorithm for deriving the vessel with suppressed local changes in thickness. Distance transformed images were obtained from the segmented vessels, and then the skeleton images with distance values, i.e., vessel thickness, were determined by logical AND operation between the skeleton image and the distance-transformed image.[16,17] By use of a reverse distance transformation of the skeleton image with distance values, the original segmented vessel can be recovered.[18] However, if the local changes in vessel thickness caused by aneurysms are suppressed by smoothing of the skeleton image with a rind filter, a vessel with suppressed local changes in thickness was produced instead of the original vessel. The rind filter was a hollow-sphere filter with a one-voxel rind, where the rind region had a value of one and the inside region had a value of zero. By use of the rind filter, the voxel value at the center of the sphere was replaced by the maximum distance value within the rind region. The diameter of the rind filter was determined to be three times larger than the maximum distance value on the skeleton image within the candidate region.

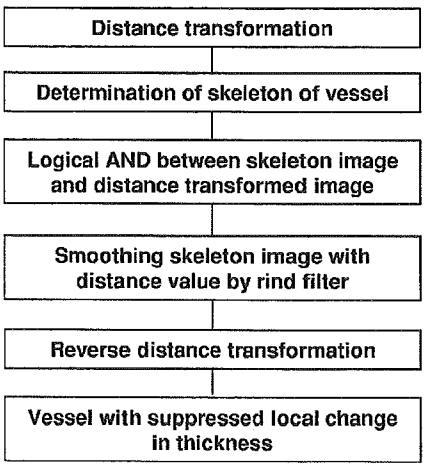

FIG. 5. Algorithm for deriving the vessel with suppressed local change in vessel thickness.

E. Feature extraction of small protrusion based on SBDI technique

The SBDI technique is used for extracting useful image features from SBD regions, which could be small aneurysm regions for true positives, but thin or very small regions for false positives. The thickness of a vessel with a small aneurysm could be larger in the aneurysm region than in other regions, and thus an extracted SBD region would be a small aneurysm region, and the sphericity of the SBD region could be relatively high. On the other hand, in a vessel without an aneurysm, which is a false positive in this study, the local change in vessel thickness would be very small. As a result, the SBD region could be a thin or very small region, and thus the sphericities of the SBD regions obtained from the false positives could be smaller than those of aneurysms. Therefore, it is possible to remove some false positives among aneurysm candidates by using image features extracted from SBD regions. From the SBD regions and original images, we determined seven image features, i.e., effective diameter, sphericity, relative SD of the distance value between centroid and surface, maximum and minimum distance value between centroid and surface, contrast, average voxel value, and SD of the voxel value, which were used for rule-based schemes and LDA.

However, because the large type and short branch type of aneurysms are branches from a parent vessel on the skeleton image, as shown in Fig. 3, there were small local changes in the thicknesses of parent vessels. Therefore, we applied the SBDI technique only to the single-vessel type and bifurcation type.

F. False positive removal based on rule-based schemes and LDA

For the removal of false positives, all rules used in rule-based schemes were automatically determined based on image features of all training aneurysms in each category (Fig. 3) by the use of simple thresholdings, such as 5% higher and 5% lower than the maximum and minimum values of each feature.

The LDA was applied for the further removal of false positives. The LDA is one of multivariate analysis methods. The basic idea of the LDA is to discriminate between two groups based on an output of a linear discriminant function (LDF) derived from the data of two groups (e.g., Group A and B), and then to classify unknown data into one of the two groups. The unknown data is classified by thresholding the output of the LDF (e.g., if the output was plus, the unknown data would be determined to belong to a Group A). In this study, the LDF was derived from four image features (variables) of all cases except one case, and then all candidates in the case left out was classified with the LDF into aneurysm-candidate group and false-positive group.

The number of features for the short-branch-type candidates was limited, because the candidate regions were identified based on short branches in the skeleton images, not on the dot-enhanced image. Therefore, image features related to dot-enhanced images were not obtained for short-branch-

type candidates. Consequently, seven common features for short-branch-type candidates and for the other candidates can be used for the LDA. However, an effective image feature combination was chosen by use of a stepwise selection method based on Wilks' lambda and the Az value. Wilks' lambda is defined by the ratio of within-group variance to the total variance,[19] which indicates the degree of discrimination between true positives and false positives, and Az value is the area under the receiver operating characteristic (ROC) curve, which indicates an accuracy for detection of aneurysms. An initial combination of features was obtained in the stepwise method, and then an effective feature combination was selected from the initial combination of features based on the highest Az value. In the stepwise method, each feature was added or removed one by one by the use of two thresholds on the F value, one for removal and another for addition, by use of the F value, which is based on Wilks' lambda.[20] For this procedure, we employed 29 cases with 36 unruptured aneurysms and 31 nonaneurysm cases used in the previous study,[12] which was a part of Database A described in the next section. As a result, the final combination consisted of four features, i.e., the average voxel value, the relative SD of the voxel value, the relative SD of the distance between the centroid and the surface, and the difference between the maximum and minimum distance (between the centroid and the surface).

G. Subjects

We employed two databases obtained from different institutions, i.e., 53 cases with 61 aneurysms (diameter: 3–26 mm, mean of 6.6 mm) and 62 nonaneurysm cases obtained from a Siemens 1.5 T unit (Database A), and 34 cases with 36 aneurysms (1–15 mm, mean of 5.2 mm) and 29 nonaneurysm cases from a Toshiba 1.5 T unit (Database B). All aneurysms were diagnosed by digital subtraction angiography, computed tomographic angiography, surgery, or by MRA that was assessed by two experienced neuroradiologists.

Database A: MRA axial images with 512×512 pixels and a pixel size of 0.391 or 0.410 mm were acquired from 115 patients on a 1.5 T MRI scanner (Magnetom Vision, Siemens Medical Systems, Erlangen, Germany) by use of a 3-D time-of-flight (3D-TOF) technique in the Department of Radiology, Kumamoto University. The 3-D MRA images included 64, 96, or 128 slices with a slice thickness of 1.0, 0.67, or 0.5 mm, respectively. An isotropic 3-D image was $400 \times 400 \times 128$ voxels with a voxel size of 0.5 mm produced from the original 3-D MRA images by use of linear interpolation and/or cropping.

Database B: Sixty-three cases were acquired on a 1.5 T MRI scanner (Excelart, XG SPIN Edition, Toshiba Medical Systems, Tochigi, Japan) by means of a 3-D-TOF technique in the Department of Radiology, Kyorin University. Original 3-D MRA images with a pixel size of 0.3906 or 0.4167 mm and a slice thickness of 1.0 or 1.1 mm were converted into isotropic 3-D images with $400 \times 400 \times 120$–$160$ voxels and a voxel size of 0.5 mm by the use of linear interpolation and/or cropping.

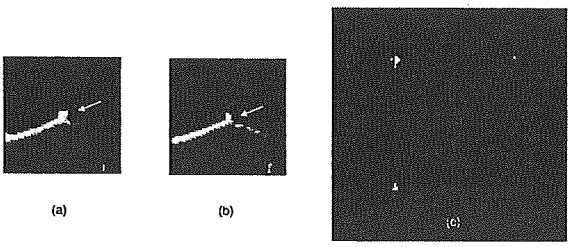

FIG. 6. An illustration of (a) an original segmented vessel with an aneurysm, (b) a vessel with a suppressed aneurysm, and (c) a cross section of an SBD region in coronal (top left), sagittal (top right), and axial (bottom left) planes.

H. Evaluation of the performance

The performance of our CAD scheme was evaluated for Database A based on a FROC curve, whereas the robustness of the scheme was estimated for the independent Database B. We tested our CAD scheme for the two databases separately with a leave-one-out-by-patient test method. Because each database was relatively small, we needed to use as many cases as possible for the robust training of the CAD scheme. However, if databases for testing were very large, a half-and-half split test or n-way cross-validation test would be more appropriate.

With this test method, all aneurysm candidates except those from one patient were used for training with two rule-based schemes and the linear discriminant function, and the candidates left out were used for testing. This procedure was repeated for all patients, so that all candidates in each patient were used once as test candidates. By changing a threshold value for discriminant scores of the candidates produced with the linear discriminant function, which was determined by LDA for distinction between aneurysms and false positives, we determined the FROC curve of the CAD scheme. For obtaining the FROC curve, we sequentially applied rule-based schemes and LDA to all candidates based on the leave-one-out-by-patient test method.

III. RESULTS AND DISCUSSION

The effects of the SBDI technique on a true positive and a false positive, i.e., the vessel with and without an aneurysm, are shown in Figs. 6 and 7, respectively. By use of the SBDI technique, the vessel with a suppressed local change in vessel thickness was derived, as shown in Fig. 6(b) from the original segmented vessels with an aneurysm (bifurcation type), as shown in Fig. 6(a). Although the thicknesses of some portions of the vessel changed from the original one, as shown in Fig. 6(b), an aneurysm was suppressed effectively. As a result, the SBD region was extracted from the parent vessel as an aneurysm region, as shown in Fig. 6(c). On the other hand, for the false positive in Fig. 7, the original vessel as shown in Fig. 7(a) was similar to the vessel with suppressed local change in vessel thickness as shown in Fig.

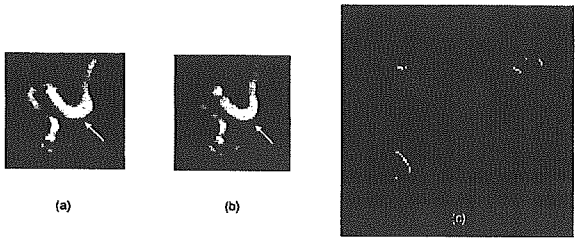

FIG. 7. An illustration of (a) an original segmented vessel without an aneurysm (false positive), (b) vessel with suppressed local change in vessel thickness, and (c) cross section of an SBD region in coronal (top left), sagittal (top right), and axial (bottom left) planes.

7(b), because the local changes in the vessel thickness without aneurysms were small. Consequently, the difference between the original and suppressed images, i.e., the SBD region, was very small, as shown in Fig. 7(c).

Figure 8 shows the relationship between the effective diameter and sphericity of candidates of the single vessel type for Database A. The sphericities of many false positives were smaller than those of aneurysms, because only thin rind regions or tiny regions could have remained for the false positives as SBD regions as shown in Fig. 7(c), whereas small protrusions with a semispherical shape would have been extracted for small aneurysms, as shown in Fig. 6(c). Furthermore, the effective diameters of some false positives were relatively smaller than those of many aneurysms, except one aneurysm. Therefore, many false positives can be eliminated by the use of some appropriate rules.

Figure 9 shows the FROC curve for the overall performance of our scheme for Database A by the use of LDA with the leave-one-out-by-patient test method. For producing the FROC curve with the SBDI technique, we applied our scheme to the candidates at an operating point without the SBDI technique, i.e., the sensitivity was 97% with 5.8 false positives per patient. As a result, our scheme achieved the

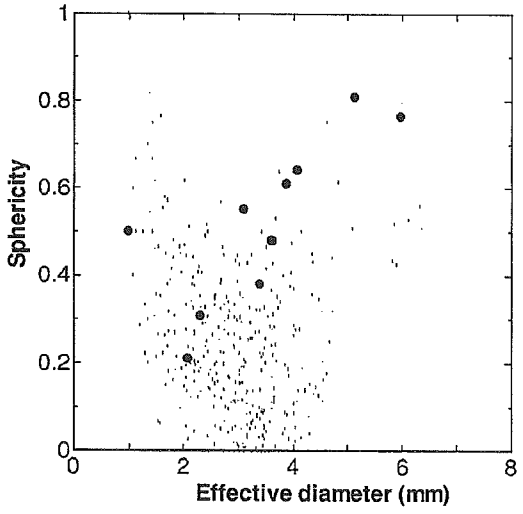

FIG. 8. The relationship between the effective diameter and sphericity of candidates of a single vessel type for Database A.

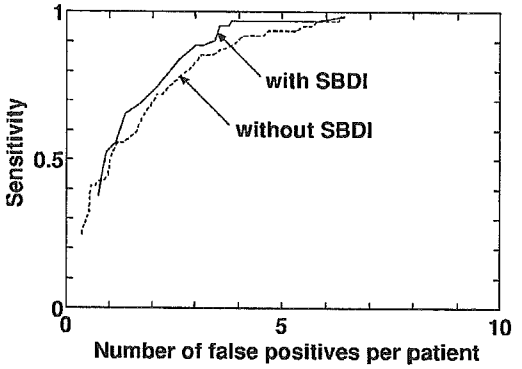

FIG. 9. FROC curve for the overall performance of our scheme for Database A by use of LDA with the leave-one-out-by-patient test method.

same sensitivity of 97% with 3.8 false positives per patient for 115 cases. The SBDI technique was applied to only the bifurcation type and single vessel type of candidates. The total number of the bifurcation type and single vessel type of false positives per patient decreased by 53% compared with the result without the SBDI technique. This result shows that the SBD image features would be effective for removing the bifurcation type and single-vessel type of false positives.

To evaluate the robustness of our scheme, we tested our scheme for an independent different database with different aneurysm sizes, i.e., Database B acquired from a Toshiba MRI scanner at Kyorin University. In the leave-one-out-by-patient method test, all rules for false positive removal were automatically determined from the image features of aneurysms included in Database B, but the other parameters of the scheme (e.g., the minimum effective diameter for initial candidates, thickness and diameter of the hollow rind filter) were the same as used for Database A. The image features on LDA were the same as used for Database A. As a result, the best performance of our CAD scheme for Database B indicated a sensitivity of 94% with 2.3 false positives per patient. This result may show that our scheme would be robust for a different database acquired by a different MRI scanner at a different institute if the rules for the CAD system would be retrained appropriately at each institution. We believe that most CAD systems would require retraining of rules for the detection of aneurysms in practical use at each institution, because the CAD performance varies depending on the image quality of MRA, which could differ by institution and MRI scanner. However, the method for retraining of the rules should be relatively simple or be automated, as described in Sec. II F. Nevertheless, for a further investigation of the robustness of our scheme, our CAD scheme needs to be applied to several independent databases acquired from different MRI scanners with different magnitudes of magnetic field at different institutions.

Undersampling for small aneurysms, i.e., larger slice thickness compared with small aneurysms, could affect the CAD performance. However, the slice thickness should be determined according to the minimum diameter of target aneurysms. In a previous study, we focused on aneurysms

equal to or larger than 3.0 mm, because the possibility of rupture for aneurysms smaller than 3.0 mm would be uncertain. However, for investigating the potential of our CAD scheme for very small aneurysms, in this study, we applied it to Database B, including ten aneurysms equal to or smaller than 2 mm, where two aneurysms were 1 mm and eight aneurysms were 2 mm. For detecting small aneurysms with 1 and 2 mm diameters, the sampling intervals should be smaller than 0.5 and 1 mm, respectively. However, the original slice thickness in the Database B was 1.0 or 1.1 mm, which was undersampling for such very small aneurysms, although the voxel size after linear interpolation was 0.5 mm. Nevertheless, the CAD scheme was able to detect one of two 1 mm aneurysms and seven of eight 2 mm aneurysms, and the sensitivity was 80% for such very small aneurysms. We believe that if the original slice thickness was smaller than 0.5 mm, the performance of our CAD scheme would be higher. Therefore, this result showed the potential of our CAD scheme for the detection of very small aneurysms.

In conclusion, we have improved a computerized scheme for the detection of intracranial aneurysms for 3-D MRA based on the SBDI technique. While keeping a high sensitivity of 97%, the number of false positives per patient decreased by 2.0 (from 5.8 to 3.8) by use of the SBDI technique. Our scheme may be robust and useful in assisting radiologists for detecting aneurysms at 3-D MRA for various aneurysm sizes and image qualities.

ACKNOWLEDGMENTS

The authors are grateful to Mitsue Miyazaki, Ph.D., Toshiba Corporation, for her useful discussion, and Ms. Elisabeth Lanzl for improving the manuscript. This work is supported in part by USPHS Grants No. CA 61625 and No. CA 98119. S. Katsuragawa and K. Doi are shareholders of R2 Technology, Inc., Los Altos, CA. CAD technologies developed in the Kurt Rossmann Laboratories have been licensed to companies including R2 Technology, Deus Technologies, Riverain Medical Group, Mitsubishi Space Software Co., Median Technologies, General Electric Corporation, and Toshiba Corporation. It is the policy of The University of Chicago that investigators disclose publicly actual or potential significant financial interests that may appear to affect research activities or that may benefit from research activities.

APPENDIX: DEFINITIONS OF IMAGE FEATURES SHOWN IN TABLE I

The image features shown in Table I are defined in this appendix.

Gray level features:

(1) Average voxel value: Average voxel value within a segmented region.
(2) Standard deviation (SD) of voxel value: SD of voxel value within a segmented region.
(3) Relative contrast to average voxel value: Difference between maximum and minimum voxel values divided by average voxel value within a segmented region.
(4) Relative difference in SD of voxel values between candidate and outside regions: Difference in SD of voxel values between candidate and outside regions divided by the SD within a candidate region. The candidate and outside regions for each candidate were defined by the candidate region at a current gray level threshold and the increased region at the subsequent gray level threshold in region growing technique, respectively.
(5) Relative difference in average voxel values between candidate and outside regions: Difference in average voxel values between candidate and outside regions divided by average voxel value within a candidate region.

Morphological features:

(1) Effective diameter: Diameter of a sphere with the same volume as that of the candidate.
(2) Sphericity: Fraction of the overlap volume between the candidate region and the sphere with the same volume as the candidate volume.
(3) Relative SD of the distance between centroid and surface: SD of Euclidean distance value between centroid and surface voxels in terms of candidate region divided by average distance value.
(4) Maximum and minimum distance between centroid and surface: Maximum and minimum Euclidean distance between centroid and surface voxels.
(5) Difference between maximum and minimum distance between centroid and surface: Difference between maximum and minimum Euclidean distance between centroid and surface voxels.
(6) Maximum or average distance value of distance-transformed image: Maximum or average distance value of distance-transformed image derived from a segmented region with a candidate in the original image.
(7) Relative difference in maximum distance between candidate and outside regions: Difference in maximum distance value of distance-transformed image between candidate and outside regions divided by the maximum distance within the candidate region.
(8) Length of protrusion: Difference between the short-branch length in the skeleton image and the radius of a parent vessel obtained from the distance-transformed image.

[a]Address correspondence to: Hidetaka Arimura, Ph.D., Department of Health Sciences, School of Medicine, Kyushu University, 3-1-1, Maidashi, Higashi-ku, Fukuoka 812-8582, Japan. Electronic mail: arimura@shs.kyushu-u.ac.jp

[1]J. T. King Jr., "Epidemiology of aneurysm subarachnoid hemorrhage," Neuroimaging Clin. N. Am. **7**, 659–668 (1997).
[2]J. M. Wardlaw and P. M. White, "The detection and management of unruptured intracranial aneurysms," Brain **123**, 205–221 (2000).
[3]S. Juvela, M. Porras, and K. Poussa, "Natural history of unruptured intracranial aneurysms: probability of and risk factors for aneurysm rupture," J. Neurosurg. **93**, 379–87 (2000).

[4]H. P. Chan, K. Doi, C. J. Vyborny, R. A. Schmidt, C. E. Metz, K. L. Lam, T. Ogura, Y. Wu, H. MacMahon, and E. A. Sickles, "Improvement in radiologists' detection of clustered microcalcifications on mammograms—The potential of computer-aided diagnosis," Invest. Radiol. **25**, 1102–1110 (1990).
[5]Z. Huo, M. L. Giger, C. J. Vyborny, and C. E. Metz, "Effectiveness of CAD in the diagnosis of breast cancer: An observer study on an independent database of mammograms," Radiology **224**, 560–568 (2002).
[6]H. Arimura, S. Katsuragawa, K. Suzuki, F. Li, J. Shiraishi, and K. Doi, "Computerized scheme for automated detection of lung nodules in low-dose CT images for lung cancer screening," Acad. Radiol. **11**, 617–629 (2004).
[7]Y. Uchiyama, S. Katsuragawa, H. Abe, J. Shiraishi, F. Li, Q. Li, C.-T. Zhang, K. Suzuki, and K. Doi, "Quantitative computerized analysis of diffuse lung disease in high-resolution computed tomography," Med. Phys. **30**, 2440–2464 (2003).
[8]F. Li, H. Arimura, K. Suzuki, J. Shiraishi, Q. Li, H. Abe, R. Engelmann, S. Sone, H. MacMahon, and K. Doi, "Computer-aided detection of peripheral lung cancers missed at CT: ROC analyses without and with localization," Radiology **237**, 684–690 (2005).
[9]H. Yoshida, Y. Masutani, P. MacEneaney, D. Rubin, and A. H. Dachman, "Computerized detection of polyps in CT colonography," Radiology **222**, 327–336 (2002).
[10]J. Nappi and H. Yoshida, "Feature-guided analysis for reduction of false positives in CAD of polyps for CT colonography," Med. Phys. **30**, 1592–1601 (2003).
[11]K. Doi, "Current status and future potential of computer-aided diagnosis in medical imaging," Br. J. Radiol. **78**, S3–S19 (2005).
[12]H. Arimura, Q. Li, Y. Korogi, T. Hirai, H. Abe, Y. Yamashita, S. Katsuragawa, R. Ikeda, and K. Doi, "Automated computerized scheme for detection of unruptured intracranial aneurysms in three-dimensional MRA," Acad. Radiol. **11**, 1093–1104 (2004).
[13]T. Hirai, Y. Korogi, H. Arimura, S. Katsuragawa, M. Kitajima, M. Yamura, Y. Yamashita, and K. Doi, "Intracranial aneurysms at MR angiography: Effect of computer-aided diagnosis on radiologists' detection performance," Radiology **237**, 605–610 (2005).
[14]Q. Li, S. Sone, and K. Doi, "Selective enhancement filters for nodules, vessels, and airway wall in two- and three-dimensional CT scans," Med. Phys. **30**, 2040–2051 (2003).
[15]H. Arimura, Q. Li, Y. Korogi, T. Hirai, H. Abe, Y. Yamashita, S. Katsuragawa, R. Ikeda, and K. Doi, "Development of CAD scheme for automated detection of intracranial aneurysms in magnetic resonance angiography," *18th International Congress of CARS—Computer Assisted Radiology and Surgery*, Chicago, USA, ICS, 2004, Vol. 1268, pp. 1015–1020.
[16]T. Saito and J. Toriwaki, "New algorithms for Euclidean distance transformations of an n-dimensional digitized picture with applications," Pattern Recogn. **27**, 1551–1565 (1994).
[17]T. Saito and J. Toriwaki, "A sequential thinning algorithm for three dimensional digital pictures using the Euclidean distance transformation," *Proc. 9th Scandinavian Conf. Image Analysis*, SCIA'95, 1995, pp. 507–516.
[18]G. Borgefors, K. I. Nystro, and G. S. D. Baja, "Computing skeletons in three dimensions," Pattern Recogn. **32**, 1225–1236 (1999).
[19]R. A. Johnson and D. W. Wichern, *Applied Multivariate Statistical Analysis* (Prentice-Hall, Englewood Cliffs, NJ, 1992), Sec. 5.3, pp. 184–188.
[20]M. Aoyama, Q. Li, S. Katsuragawa, H. MacMahon, and K. Doi, "Automated computerized scheme for distinction between benign and malignant solitary pulmonary nodules on chest images," Med. Phys. **29**, 701–708 (2002).

Radiology

Toshinori Hirai, MD
Yukunori Korogi, MD
Hidetaka Arimura, PhD
Shigehiko Katsuragawa, PhD
Mika Kitajima, MD
Masayuki Yamura, MD
Yasuyuki Yamashita, MD
Kunio Doi, PhD

Published online before print
10.1148/radiol.2372041734
Radiology 2005; 237:605–610

Abbreviations:
A_z = area under receiver operating characteristic curve
CAD = computer-aided detection
MIP = maximum intensity projection

[1] From the Department of Diagnostic Radiology, Graduate School of Medical Sciences, Kumamoto University 1-1-1 Honjo, Kumamoto 860-8556, Japan (T.H., S.K., M.K., M.Y., Y.Y.); Department of Radiology, University of Occupational and Environmental Health, School of Medicine, Kitakyushu, Japan (Y.K.); Department of Health Sciences, Kyushu University, Fukuoka, Japan (H.A.); and Department of Radiology, University of Chicago, Chicago, Ill (K.D.). Received October 9, 2004; revision requested December 20; revision received January 6, 2005; accepted January 25. **Address correspondence to** T.H. (e-mail: *toshinor@beige.ocn.ne.jp*).

Authors stated no financial relationship to disclose.

Author contributions:
Guarantors of integrity of entire study, T.H., Y.K., H.A., S.K., K.D.; study concepts/study design or data acquisition or data analysis/interpretation, all authors; manuscript drafting or manuscript revision for important intellectual content, all authors; approval of final version of submitted manuscript, all authors; literature research, T.H.; clinical studies, H.A., S.K., M.K., M.Y.; statistical analysis, T.H., S.K.; and manuscript editing, T.H., Y.K., H.A., S.K., Y.Y., K.D.

Intracranial Aneurysms at MR Angiography: Effect of Computer-aided Diagnosis on Radiologists' Detection Performance[1]

PURPOSE: To retrospectively evaluate the effect of computer-aided detection (CAD) on radiologists' performance in detection of intracranial aneurysms with magnetic resonance (MR) angiography.

MATERIALS AND METHODS: The institutional review board approved this study and did not require patient informed consent. Fifty maximum intensity projection MR angiograms in 50 patients were used for observer performance study. The group included 22 patients (age range, 43–86 years; mean, 60.2 years; 6 men and 16 women) with intracranial aneurysms and 28 patients (age range, 32–80 years; mean, 58.8 years; 10 men and 18 women) without aneurysms. The MR angiograms were obtained with three-dimensional time-of-flight 1.5-T MR imaging. Fifteen radiologists, including eight neuroradiologists and seven general radiologists, participated in the observer performance test. They interpreted the angiograms first without and then with the aid of the computer output by using an automated computerized scheme. The observers' performance without and with the computer output was evaluated with receiver operating characteristic analysis.

RESULTS: For all 15 observers, average area under the receiver operating characteristic curve (A_z) value for detection of aneurysms was increased significantly from 0.931 to 0.983 ($P = .001$) when they used the computer output. A_z values for general radiologists and neuroradiologists increased from 0.894 to 0.983 ($P = .022$) and from 0.963 to 0.984 ($P = .014$), respectively. Improvement in the performance of general radiologists in terms of the A_z value was much greater than that of neuroradiologists. Performance of general radiologists with CAD ($A_z = 0.983$) slightly exceeded that of neuroradiologists without CAD ($A_z = 0.963$) ($P = .048$).

CONCLUSION: CAD improved neuroradiologists' and general radiologists' performance for detection of intracranial aneurysms with MR angiography; improvement was greater for general radiologists than it was for neuroradiologists.

The natural history of unruptured intracranial aneurysms is not completely understood. Findings at autopsy and angiographic studies showed that between 3.6% and 6% of the general population harbor an unruptured intracranial aneurysm (1). The analytic results of the International Study of Unruptured Intracranial Aneurysms indicated that the risk of rupture is related to the site and size of an aneurysm and to a history of subarachnoid hemorrhage (2). With regard to treatment for unruptured intracranial aneurysms, benefits of surgical treatment or of endovascular intervention have been suggested in some studies (3,4). Recently, the investigators of the International Study of Unruptured Intracranial Aneurysms proposed that the specific risks related to the natural history of intracranial aneurysms should be considered in the treatment of each patient (5).

Magnetic resonance (MR) angiography is a widely available and noninvasive imaging modality that has high sensitivity for the detection of intracranial aneurysms. The accuracy of MR angiography in the detection of intracranial aneurysms is about 90% (6). The sensitivity of MR angiography was greater for detection of aneurysms larger than 3 mm than it was for detection of aneurysms that were 3 mm or smaller, that is, 94% versus 38% (6).

During the past 10 years, screening of unruptured intracranial aneurysms with MR angiography has gained attention, for example, for examining asymptomatic patients who are at risk of having an aneurysm because of a strong family history of aneurysmal subarachnoid hemorrhage or because of autosomal dominant polycystic kidney disease (7–9). Although screening of asymptomatic individuals without such risk factors is still controversial, MR angiography is used for screening of unruptured aneurysms in the general population in Japan (10).

To date, MR angiography is widely accepted in screening for intracranial aneurysms, and the demand is increasing. In screening for unruptured intracranial aneurysms with MR angiography, however, radiologists need to analyze large amounts of data that include multiple image projections per examination and source images obtained with MR angiography. It is time consuming and sometimes difficult for radiologists to find small aneurysms, or it may not be easy to detect medium aneurysms on maximum intensity projection (MIP) images, because of overlap with adjacent vessels and because of unusual locations (11,12). Thus, there is always the risk of missing an aneurysm. There are some methods that help avoid missing an intracranial aneurysm, such as the use of independent readings by two or more radiologists (11). Independent readings by two or more radiologists, however, increase the workload of radiologists in a routine clinical practice.

In regard to other organs, the concept of computer-aided detection (CAD) for screening of breast cancer with mammography and for screening of lung cancer with chest radiography and/or computed tomography (CT) has been applied, and the usefulness of CAD systems for the detection of cancers has been reported (13–17). To our knowledge, however, a CAD scheme has not been applied to the detection of intracranial aneurysms with MR angiography. We have been developing a CAD system for detection of intracranial aneurysms in screening with MR angiography (18). The purpose of our study, therefore, was to retrospectively evaluate the effect of CAD on radiologists' performance in the detection of intracranial aneurysms with MR angiography.

MATERIALS AND METHODS

Patient Selection

One neuroradiologist (T.H.) retrospectively selected 60 consecutive patients with unruptured intracranial aneurysms who underwent MR angiography at the Kumamoto University Hospital, Kumamoto, Japan, to evaluate possible intracranial vascular lesions between October 1999 and August 2003. The patients' data were derived from the MR imaging database of our institution. From the same database, 60 age-matched patients without intracranial aneurysms were also recruited by the same neuroradiologist. MR angiograms obtained in the 120 patients were reviewed in consensus by two experienced neuroradiologists (T.H. and Y.K., with 16 and 24 years of experience, respectively) who did not participate in the observer performance study. Our institutional review board approved this study and did not require patient informed consent.

MR Imaging

All MR imaging examinations were performed with a 1.5-T imager (Magnetom Vision; Siemens Medical Systems, Erlangen, Germany) by using a circular polarized head coil. Three-dimensional time-of-flight MR angiograms were obtained with the following parameters: 32/6 (repetition time msec/echo time msec), one signal acquired, 20° flip angle, 64-mm slab thickness, 64 partitions, 20-cm field of view, and 256 × 512 matrix. The acquisition data were converted into a 512 × 512 matrix, with a pixel size of 0.39 × 0.39 mm, by using an interpolation technique. Tilted optimized nonsaturating excitation and magnetization transfer pulses were applied for enhancement of the signals of blood flow. The slabs were placed to include the structures from the intracranial vertebral artery to the A2 branch of the anterior cerebral artery. Saturation pulses were applied cephalad so that venous blood signals were eliminated.

Selection for Observer Performance Study

Twenty-two of the 60 patients with unruptured intracranial aneurysms were further selected for an observer performance study by the same two neuroradiologists who performed the patient selection. The inclusion criteria for the patient selection were as follows: *(a)* patients with only one aneurysm were chosen, *(b)* location and size of the aneurysm were similar to the distributions in a clinical environment, and *(c)* high-quality MR angiograms were available for interpretation. There were six men and 16 women, with an age range of 43–86 years (mean age, 60.2 years). The locations and sizes of the aneurysms are listed in Table 1. The sizes of the aneurysm ranged from 3 to 26 mm in maximum diameter (mean, 7.1 mm). According to the maximum diameter, the aneurysms were classified into three groups: eight small (<5 mm), 11 medium (5–12 mm), and three large (>12 mm). The aneurysms were located at the internal carotid artery (n = 10), middle cerebral artery (n = 4), anterior cerebral artery (n = 3), basilar artery (n = 3), posterior cerebral artery (n = 1), and vertebral artery (n = 1). The 22 lesions included 20 saccular aneurysms and two fusiform aneurysms. The diagnosis was proved at CT angiography (n = 12) and conventional digital subtraction angiography (n = 3); the remaining seven aneurysms were confirmed with consensus reading of MR angiograms by the same two experienced neuroradiologists mentioned before. Source images obtained with MR angiography were also used for the confirmation. Eight of the 22 patients had old brain infarctions; intracranial steno-occlusive disease was present in two patients. An azygous anterior cerebral artery was seen in one patient with a distal anterior cerebral artery aneurysm. Meningioma and pituitary microadenoma were seen on conventional MR images in one case each. These additional lesions did not affect the interpretation of MR angiograms.

Twenty-eight of the 60 patients without intracranial aneurysms were further selected by the same two neuroradiologists as a control group for the observer study, and the age information was similar to that of the group with aneurysms. The diagnosis of no intracranial aneurysms was proved with consensus reading of MR angiograms by the two experienced neuroradiologists; source images obtained with MR angiography were also used for the diagnosis. There were 10 men and 18 women, with an age range of 32–80 years (mean age, 58.8 years). Four of the 28 patients had old brain infarctions that did not affect the image interpretation. There were no other apparent brain lesions on MR images in this control group.

TABLE 1
Location and Size of Aneurysms

Location	Size			Total No. of Patients
	Small	Medium	Large	
Internal carotid artery, top portion	0	1	0	1
Internal carotid and anterior choroidal arteries	1	0	0	1
Internal carotid and posterior communicating arteries	1	0	0	1
Internal carotid artery, first part of cisternal segment and carotid knee segment	1	1	0	2
Internal carotid and ophthalmic arteries	1	0	0	1
Internal carotid artery, carotid knee segment	1	0	0	1
Internal carotid artery, cavernous segment	0	1*	2	3
Middle cerebral artery, sphenoidal and insular segments	2	1	1	4
Anterior communicating artery	0	2	0	2
Anterior cerebral artery, distal portion	0	1	0	1
Posterior cerebral artery, distal portion	0	1	0	1
Basilar artery, top portion	0	1	0	1
Basilar and anterior inferior cerebellar arteries	0	1	0	1
Basilar artery	1	0	0	1
Vertebral artery	0	1*	0	1
Total	8	11	3	22

* Fusiform aneurysm.

TABLE 2
A_z Values for Radiologists in Detection of Intracranial Aneurysms

Observers	Without CAD	With CAD
Neuroradiologists		
1	0.939	0.964
2	0.986	0.994
3	0.989	0.998
4	0.969	0.970
5	0.969	0.984
6	0.952	0.993
7	0.942	1.000
8	0.958	0.967
Mean	0.963	0.984
General radiologists		
9	0.916	0.961
10	0.909	0.984
11	0.871	0.978
12	0.909	0.989
13	0.871	0.989
14	0.872	0.984
15	0.910	0.993
Mean	0.894	0.983
Overall	0.931	0.983

Computerized Scheme for Automated Detection of Intracranial Aneurysms

Details of the CAD scheme used in this study are shown elsewhere (18). First, the isotropic images from three-dimensional MR angiography were processed by using three selective filters for enhancement of aneurysms, vessels, and vessel walls. The initial candidates were identified by using a multiple gray-level threshold technique on the three-dimensional dot-enhanced images within the search area, which was determined with dilatation of major vessels, because most aneurysms appear in specific vessels. Candidate regions were segmented by using a region-growing technique with monitoring of some image features. In the next step, all candidates were classified into four types according to the size of the aneurysms and the local structures involved. In each group, a number of nonaneurysms were removed by using rules that were based on localized image features related to gray levels and morphologic characteristics. Finally, linear discriminant analysis was employed for further removal of some false-positive findings. Our scheme achieved a sensitivity of 100% (36 of 36), with 0.55 false-positive finding per patient in a consistency test (18).

Observer Performance Study

A total of 15 observers, including eight board-certified radiologists who specialized in neuroradiology (neuroradiologists) (M.K., M.Y.) and seven board-certified radiologists who did not specialize in neuroradiology (general radiologists), took part in the observer performance study. All observers were blinded to the results of the diagnosis obtained from the consensus of the two experienced neuroradiologists (T.H., Y.K.). The neuroradiologists had 8–17 years of experience (mean, 13.0 years), and the general radiologists had 7–20 years of experience (mean, 13.3 years). The sequential test method (19) was used in the observer performance study. Each observer read the MR angiograms displayed on a monitor first without the computer output and rated his or her confidence level in determining the presence or absence of an aneurysm. Next, the computer output, marked by circles that indicated potential aneurysms, was superimposed on the MR angiograms. The observer then viewed the image with the computer output and rated it again. An interface program was created for an image display without and with the computer output for the observer performance test. The 15 observers viewed the MIP MR angiograms displayed on a gray-scale monitor (Precision 650; Dell, Round Rock, Tex) with a spatial resolution of 1600 × 1200. The monitor screen was divided into two areas: one area in which MR angiograms were displayed in z-axis, x-axis, and y-axis rotations and another area in which observers indicated their confidence levels in the observer performance study. On the monitor, observers could see 19 MIP MR angiograms ranging from −90° to +90° (10° intervals) in the z-axis rotation and five MIP MR angiograms ranging from −20° to +20° (10° intervals) in the x-axis and y-axis rotations. The observers were allowed to select the direction of the MR angiograms and the magnification of the images on the monitor. They were also permitted to use the cine mode for displaying the images.

Images in all of the 50 patients (22 with aneurysms and 28 without aneurysms) selected for the observer performance study were presented in the same randomized order to the observers. The observers were provided with the following information before the observer performance test: *(a)* the sequential test method that was used, *(b)* there was only one aneurysm in each patient, and *(c)* the type of aneurysm was either saccular or fusiform. The observers were blinded to the number of patients with aneurysms and the performance level of the CAD scheme. There was no limit on the reading time.

Before the observer performance test, each observer underwent a training session with four training cases to become familiar with the computer output and the test procedure. The four training cases were not included with the images from the 50 selected patients used in the

observer performance study. Each observer used a continuous rating scale of a line-marking method to rate his or her confidence level on the monitor. At the left end of the line, a confidence level that an aneurysm was definitely absent was indicated, whereas at the right end, a confidence level that an aneurysm was definitely present was indicated. Intermediate levels of confidence were indicated by the different positions on the line between the two ends, and positions close to the right and left ends indicated, respectively, greater and lesser degrees of confidence in regard to the presence of an aneurysm. The distance between the left end and the marked point was automatically determined in the computer and was converted to a confidence level that could range from 0 to 100.

To investigate the effect of CAD further, we also determined the difference between the confidence levels without and with the computer output. We assumed that a clinically relevant change in confidence levels occurred only when the difference was greater than 20 units on a 0–100 confidence rating scale. A shift of more than 20 units in the direction toward a correct diagnosis implied that the use of the CAD was beneficial. Similarly, a shift of more than 20 units in the direction toward an incorrect diagnosis implied that the use of CAD was detrimental. The number of cases with beneficial effects and the number of those with detrimental effects, according to each observer, were assessed.

Statistical Analysis

Observer performance was evaluated by using receiver operating characteristic analysis with the LABROC program, according to Metz et al (20). The receiver operating characteristic curves for each observer without and with the computer output indicated the true-positive fraction to the false-positive fraction at each confidence level. The area under the receiver operating characteristic curve (A_z) was used for comparing the observers' performance in the detection of intracranial aneurysms.

To investigate the effect of CAD for all observers, the significance of the difference between the A_z values obtained without and with CAD was evaluated by using the Wilcoxon matched-pairs signed rank test. To investigate the effect of CAD for each radiologist group, the significance of the difference in A_z values between neuroradiologists and general radiologists was evaluated with a Mann-Whitney U test. In addition, the difference between the average numbers of cases affected beneficially and detrimentally because of CAD was analyzed by using the Wilcoxon matched-pairs signed rank test. In all the analyses, a P value of less than .05 was considered to indicate a significant difference.

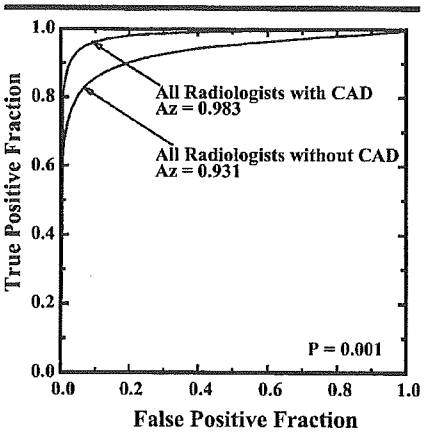

Figure 1. Graph shows average receiver operating characteristic curves for all observers in the detection of intracranial aneurysms without and with CAD output. The average A_z value in the detection of aneurysms was significantly improved from 0.931 to 0.983 when observers used the computer output (P = .001).

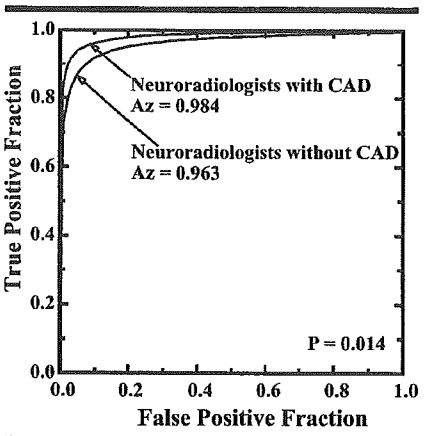

Figure 2. Graph shows average receiver operating characteristic curves for eight neuroradiologists in the detection of intracranial aneurysms. The average A_z value in detection of aneurysms was improved significantly from 0.963 to 0.984 when they used the computer output (P = .014).

RESULTS

Observer Performance

For all observers, the mean A_z values (Fig 1, Table 2) obtained without and with CAD were 0.931 ± 0.04 (standard deviation) and 0.983 ± 0.01, respectively, which indicated a significant difference (P = .001). In the neuroradiologist group (Fig 2), the mean A_z values obtained without and with CAD were 0.963 ± 0.02 and 0.984 ± 0.01, respectively, which indicated a significant difference (P = .014). In the general radiologist group (Fig 3), the mean A_z values obtained without and with CAD were 0.894 ± 0.02 and 0.983 ± 0.01, respectively, which indicated a significant difference (P = .022). There was a significant difference in the mean A_z values obtained without CAD between the two groups of radiologists (P = .001). There was no significant difference, however, in the mean A_z values obtained with CAD between the two groups of radiologists (P = .522). The performance of general radiologists (A_z = 0.983) with CAD slightly exceeded that of neuroradiologists (A_z = 0.963) without CAD. There was a significant difference in the mean A_z values between the general radiologist group with CAD and the neuroradiologist group without CAD (P = .048).

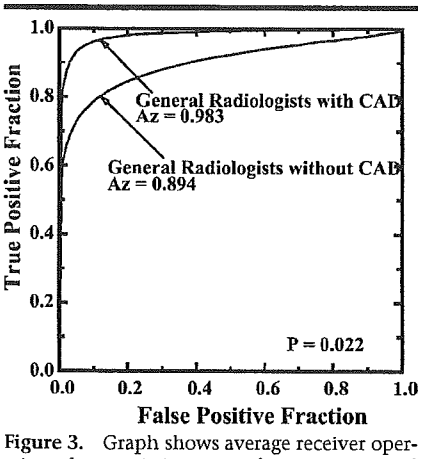

Figure 3. Graph shows average receiver operating characteristic curves for seven general radiologists in the detection of intracranial aneurysms. The average A_z value in detection of aneurysms was improved significantly from 0.894 to 0.983 when they used the computer output (P = .022).

Confidence Ratings

The results of a clinically relevant change in confidence ratings for each observer (Figs 4, 5) showed that among the 22 patients with aneurysms, the average number of cases affected beneficially was 2.3 (10%). There were no cases of patients with an aneurysm that were affected detrimentally. Among the 28 patients with-

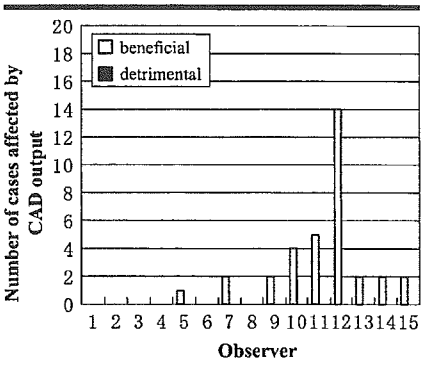

Figure 4. Graph shows number of cases (>20%) affected by the CAD output in confidence level with regard to patients with aneurysms. There were no cases affected detrimentally. The numbers *1–8* on x-axis represent the eight neuroradiologists and *9–15* represent the seven general radiologists.

TABLE 3
Summary of Aneurysms Affected Beneficially by CAD

Observers and Location	Size (mm)	No. of Cases
Neuroradiologists		
Internal carotid and anterior choroidal arteries	3	2
Internal carotid and posterior communicating arteries	4	1
General radiologists		
Internal carotid and anterior choroidal arteries	3	5
Internal carotid artery, carotid knee segment	3	1
Middle cerebral artery, sphenoidal and insular segments	4	9
Internal carotid and ophthalmic arteries	4	2
Internal carotid and posterior communicating arteries	4	1
Basilar artery	4	1
Internal carotid artery, top portion	5	2
Internal carotid artery, first part of cisternal segment and carotid knee segment	5	1
Anterior communicating artery	5	1
Posterior cerebral artery, distal portion	5	1
Anterior cerebral artery, distal portion	6	1
Vertebral artery*	6	3
Internal carotid artery, cavernous segment	16	3

* Fusiform aneurysms.

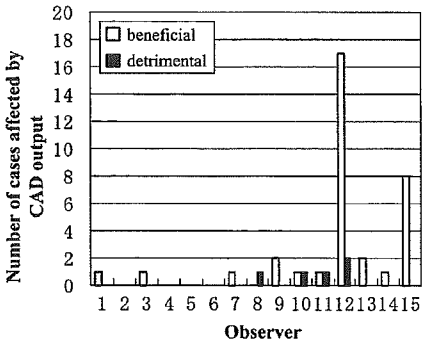

Figure 5. Graph shows number of cases (>20%) affected by CAD output in confidence level with regard to patients without aneurysms. The numbers *1–8* on x-axis represent the eight neuroradiologists, and *9–15* represent the seven general radiologists.

out aneurysms, the average number of cases that were affected beneficially was significantly larger than that of cases that were affected detrimentally (mean number of cases, 2.3 [8%] vs 0.3 [1%]; P = .02).

In beneficially affected cases in patients with aneurysms, small aneurysms at the internal carotid artery were frequently affected in both the neuroradiologist and general radiologist groups (Table 3). The general radiologists were more likely to be affected with small aneurysms at the middle cerebral artery, medium aneurysms at an unusual location such as the distal anterior and posterior cerebral arteries, medium fusiform aneurysms at the vertebral artery, and large aneurysms at the internal carotid artery. Large aneurysms at the internal carotid artery were missed in the first rating by three general radiologists because the signal intensity of the large aneurysm was relatively low as a result of turbulent flow within the aneurysm. In the five detrimentally affected cases in patients without aneurysms, the detrimental effects in both groups were caused by an increase in the confidence level in favor of the presence of an aneurysm.

DISCUSSION

We analyzed A_z values separately for neuroradiologists and general radiologists to determine whether the effect of CAD on observer performance was dependent on clinical experience. The results indicated that the use of computer output was more beneficial to general radiologists than it was to neuroradiologists; the A_z values for general radiologists with CAD were almost equal to those for neuroradiologists. In addition, it is important to note that the effect of using the computer output was also beneficial for neuroradiologists.

The knowledge required for detection of intracranial aneurysms with MR angiography includes the anatomy of the intracranial vessels, common locations of intracranial aneurysms, etiology and classification of the aneurysms, diagnostic accuracy of MR angiography for intracranial aneurysms, and artifacts and pitfalls for MR angiography. All of the general radiologists who took part in the observer study had limited experience, of 1 year or less, in neuroradiology, and were considered to be unfamiliar with findings of intracranial aneurysms. This factor presumably accounts for the finding that general radiologists benefited much more from the use of CAD. In other words, the radiologist's performance in detection of intracranial aneurysms probably depends on his or her experience and knowledge as a neuroradiologist. The fact that the effect of using CAD for neuroradiologists was also beneficial, however, may indicate that the use of CAD can improve radiologists' detection performance irrespective of their knowledge and experience.

In our study, 10% of cases in patients with aneurysms were affected beneficially by the computer output. This result was caused by an increase in the observer's confidence in diagnosing the presence of aneurysms in cases in patients with aneurysms that were detected with the use of CAD. It is sometimes difficult for radiologists to find small aneurysms, or it may not be easy to detect medium aneurysms on MIP images because of overlap with adjacent vessels and because of unusual locations (11,12). Our results without use of CAD showed a similar tendency for the false-negative findings with MIP MR angiograms. We also found that large aneurysms might be missed by general radiologists. Because general radiologists are not familiar with the unusual signal intensity of large aneurysms on MR angiograms, they might have missed these aneurysms.

Our observer performance test results indicated that the use of CAD was clearly beneficial, even in cases in patients without aneurysms. About 8% of cases in pa-

tients without aneurysms were affected beneficially because of the increase in the observer's confidence in diagnosing the absence of aneurysms in cases in patients without aneurysms. On the other hand, only 1% of cases in patients without aneurysms were affected detrimentally because of an increase in the confidence level in favor of the presence of an aneurysm. The detrimental effects were significantly smaller than were the beneficial effects. Unruptured intracranial aneurysms are being diagnosed with greater frequency as imaging technologies improve. Since the workload of radiologists will increase in the near future, the use of CAD may be necessary to increase true-positive findings and decrease false-positive findings as interpreted by radiologists.

Our study had limitations. First, source images obtained with MR angiography were not included in this observer performance study. It is likely that source images obtained with MR angiography would have been helpful in the detection of aneurysms. Reading source images obtained with MR angiography, however, may be time consuming for radiologists, especially for general radiologists. Because the fatigue in reading many images for observer performance testing may affect the results, we used only MIP images obtained with MR angiography in this study. We provided multiple views of MIP images to observers. Therefore, we believe that this observer performance test was adequate for assessment of observer performance in the detection of aneurysms. Second, this study might have had a bias in patient selection. We selected 22 patients with aneurysms and 28 control patients. The aneurysms were of various sizes, but most were small or medium, and nearly half were small. In addition, some aneurysms were located at unusual sites. Patients with steno-occlusive disease were also included to simulate patients in our routine practice. Thus, we believe that the patients we selected reflected patients seen in routine clinical practice. Third, there was a difference between the observer performance study and a clinical environment. We provided observers with the information in regard to the number of aneurysms in patients with aneurysms. Provision of such information may have affected observer performance. Although readers considered that multiple aneurysms may have existed on a given image, they indicated one aneurysm with confidence, because they knew that only one aneurysm was present in a patient with an aneurysm in the observer performance study. Thus, potential false-positive reports might have been artificially excluded.

In conclusion, the use of our CAD system helped to improve both neuroradiologists' and general radiologists' performance in the detection of intracranial aneurysms with MR angiography, and this improvement was more marked for general radiologists than it was for neuroradiologists. Further investigations about the usefulness of the CAD scheme, as applied to various MR angiograms with various MR imaging units, are needed for application in routine clinical practice.

Acknowledgments: We are grateful to the following personnel for their help: Shoji Morishita, MD, Yoshiko Hayashida, MD, Ryuji Murakami, MD, Ichiro Ikushima, MD, Yoshinori Shigematsu, MD, Takeshi Sugahara, MD, Tomoko Okuda, MD, Shingo Kakeda, MD, Takatoshi Aoki, MD, Koichi Kawanaka, MD, Yoshiharu Nakayama, MD, Masanori Imuta, MD, and Ichiro Ogata, MD, for their participation in this observer study; Junji Shiraishi, PhD, for receiver operating characteristic analysis; Roger Engelmann, MS, for development of the software used in this observer study; Ryuji Ikeda for data management; and Elisabeth Lanzl for English wording.

References

1. Wardlaw JM, White PM. The detection and management of unruptured intracranial aneurysms. Brain 2000;123:205–221.
2. International Study of Unruptured Intracranial Aneurysms Investigators. Unruptured intracranial aneurysms: risk of rupture and risks of surgical intervention. N Engl J Med 1998; 339:1725–1733.
3. Chang HS, Kirino T. Quantification of operative benefit for unruptured cerebral aneurysms: a theoretical approach. J Neurosurg 1995;83:413–420.
4. Leblanc R, Worsley KJ. Surgery of unruptured, asymptomatic aneurysms: a decision analysis. Can J Neurol Sci 1995;22: 30–35.
5. International Study of Unruptured Intracranial Aneurysms Investigators. Unruptured intracranial aneurysms: natural history, clinical outcome, and risks of surgical and endovascular treatment. Lancet 2003; 362:103–110.
6. White PM, Wardlaw JM, Easton V. Can noninvasive imaging accurately depict intracranial aneurysms? a systematic review. Radiology 2000;217:361–370.
7. Ruggieri PM, Poulos N, Masaryk TJ, et al. Occult intracranial aneurysms in polycystic kidney disease: screening with MR angiography. Radiology 1994;191:33–39.
8. Ronkainen A, Puranen MI, Hernesniemi JA, et al. Intracranial aneurysms: MR angiographic screening in 400 asymptomatic individuals with increased familial risk. Radiology 1995;195:35–40.
9. Raaymakers TW, Buys PC, Verbeeten B Jr, et al. MR angiography as a screening tool for intracranial aneurysms: feasibility, test characteristics, and interobserver agreement. AJR Am J Roentgenol 1999;173:1469–1475.
10. Baba Y, Takahashi M, Korogi Y. Cost-effectiveness of screening unruptured cerebral aneurysms in Japan. Eur Radiol 2000; 10: S362–S365.
11. Korogi Y, Takahashi M, Mabuchi N, et al. Intracranial aneurysms: diagnostic accuracy of three-dimensional, Fourier transform, time-of-flight MR angiography. Radiology 1994;193:181–186.
12. Korogi Y, Takahashi M, Mabuchi N, et al. Intracranial aneurysms: diagnostic accuracy of MR angiography with evaluation of maximum intensity projection and source images. Radiology 1996;199:199–207.
13. Freer TW, Ulissey MJ. Screening mammography with computer-aided detection: prospective study of 12,860 patients in a community breast center. Radiology 2001;220: 781–786.
14. Destounis SV, DiNitto P, Logan-Young W, Bonaccio E, Zuley ML, Willison KM. Can computer-aided detection with double reading of screening mammograms help decrease the false-negative rate? initial experience. Radiology 2004;232:578–584.
15. MacMahon H, Engelmann R, Behlen FM, et al. Computer-aided diagnosis of pulmonary nodules: results of a large-scale observer test. Radiology 1999;213:723–726.
16. Shiraishi J, Abe H, Engelmann R, Aoyama M, MacMahon H, Doi K. Computer-aided diagnosis to distinguish benign from malignant solitary pulmonary nodules on radiographs: ROC analysis of radiologists' performance—initial experience. Radiology 2003;227:469–474.
17. Awai K, Murao K, Ozawa A, et al. Pulmonary nodules at chest CT: effect of computer-aided diagnosis on radiologists' detection performance. Radiology 2004;230: 347–352.
18. Arimura H, Li Q, Korogi Y, et al. Automated computerized scheme for detection of unruptured intracranial aneurysms in three-dimensional MRA. Acad Radiol 2004;11:1093–1104.
19. Kobayashi T, Xu XW, MacMahon H, Metz CE, Doi K. Effect of a computer-aided diagnosis scheme on radiologists' performance in detection of lung nodules on radiographs. Radiology 1996;199:843–848.
20. Metz CE, Herman BA, Shen JH. Maximum-likelihood estimation of receiver operating (ROC) characteristic curves from continuously-distributed data. Stat Med 1998;17: 1033–1053.

AJNR Am J Neuroradiol 26:2243–2247, October 2005

Postoperative Assessment of Extracranial–Intracranial Bypass by Time-Resolved 3D Contrast-Enhanced MR Angiography Using Parallel Imaging

Kazuhiro Tsuchiya, Keita Honya, Akira Fujikawa, Hidekatsu Tateishi, and Yoshiaki Shiokawa

PURPOSE: **Our goals were to assess image quality of time-resolved contrast-enhanced MR angiography (CE MRA), by using 3D data acquisition along with a parallel imaging technique that can improve temporal resolution and to compare this technique with 3D-time-of-flight (TOF) MRA in the postoperative assessment of extracranial (EC)–intracranial (IC) bypass surgery.**

METHODS: **On a 1.5T imaging system, we performed CE MRA by using a 3D fast field-echo sequence in combination with a parallel imaging technique, to obtain images in the coronal plane centered at the postoperative site. Our patient group comprised 17 patients, including 13 after superficial temporal artery–middle cerebral artery (MCA) anastomosis, 3 after external carotid artery-MCA anastomosis, and one after extracranial vertebral artery–posterior cerebral artery anastomosis. Visualization of the anastomosis and the distal flow on the CE-MRA images was assessed comparatively with that on 3D-TOF MR angiograms obtained at the same time. In 6 patients, we also compared the efficiency of visualization on CE-MRA images with that on conventional angiograms.**

RESULTS: **A temporal resolution of 0.8 s/frame could be achieved with the technique employed. The bypass was better demonstrated postoperatively on CE-MRA images than on 3D-TOF MR angiograms in 13 patients (76%), whereas the 2 methods were equivalent in 4 patients (24%). Good correspondence of results was observed in the 6 patients for whom CE MRA and conventional digital subtraction angiography (DSA) images were compared.**

CONCLUSION: **CE MRA by using the parallel imaging technique can increase image acquisition speed with sufficient image quality. This technique is at least equivalent to 3D-TOF MRA to evaluate the postoperative status of EC-IC bypass.**

Extracranial–intracranial (EC-IC) bypass surgery has been used to increase the cerebral blood flow and halt extension of the affected area or reduce the risk of future strokes in patients with ischemic cerebrovascular disease (1–3). Furthermore, several kinds of bypass surgery are performed in patients with cerebral aneurysm, in which the parent artery often has to be sacrificed. In these cases, conventional angiography has been used as the most reliable method to assess the patency of the EC-IC anastomosis postoperatively. Recently, however, several other modalities—including MR angiography (MRA), sonography, and CT angiography—have also been reported to be useful for such assessment (4–7).

Time-resolved contrast-enhanced (CE) MRA, in which a rapid T1-weighted sequence is performed in combination with bolus intravenous injection of a gadolinium-based contrast agent, provides useful anatomic and hemodynamic information concerning intracranial vascular lesions. To generate "time-resolved" images, 2D sequences were previously used (8–14). More recently, however, a technique using an effective k-space sampling technique that provides good temporal resolution even with 3D data acquisition has been reported (15). Multiple arrays of receiver coils are used in the parallel imaging tech-

Received January 13, 2005; accepted after revision March 22.

From the Departments of Radiology (K.T., K.H., A.F.) and Neurosurgery (H.T., Y.S.), Kyorin University School of Medicine, Tokyo, Japan.

Presented as "Postoperative Assessment of External Carotid-Internal Carotid Bypass by MR Digital Subtraction Angiography Using Parallel Imaging"at the 42nd annual meeting of the American Society of Neuroradiology, June 7–11, 2004, Seattle, WA.

Address correspondence to Kazuhiro Tsuchiya, MD, Department of Radiology, Kyorin University School of Medicine, 6-20-2, Shinkawa, Mitaka, Tokyo 181-8611, Japan.

nique, where the imaging time is reduced by a factor equal to the number of coils used (16, 17). Application of this technique to contrast-enhanced carotid MRA has already been reported (18).

In this study, we assessed whether CE MRA with 3D data acquisition by using parallel imaging as well as an efficient method of k-space sampling might be useful in the postoperative assessment of EC-IC bypass, by providing images comparable to those obtained in conventional 3D-time-of-flight (TOF) MRA and digital subtraction angiography (DSA).

Methods

We obtained CE-MRA images from 17 consecutive patients referred to us for MR imaging following EC-IC bypass during a 2-year period. The subjects consisted of 7 men and 10 women aged 23–74 years (mean age, 51.2 years). Of these patients, 13 had undergone superficial temporal artery (STA)–middle cerebral artery (MCA) anastomosis for MCA disease (n = 8), internal carotid artery (ICA) disease (n = 2), or Moyamoya disease (n = 3), 3 had undergone external carotid artery (ECA)–MCA anastomosis for ICA disease by using a radial artery graft, and one had undergone extracranial vertebral artery (VA)–posterior cerebral artery (PCA) anastomosis by using a radial artery graft for bilateral occlusion of the vertebral arteries due to dissection and its therapy. The interval between surgery and the MR study ranged from 2 days to 4 years and 10 months (mean, 15.1 months).

On a 1.5T imaging system, in addition to obtaining conventional T1-weighted, T2-weighted, and fluid-attenuated inversion recovery (FLAIR) images, and MR angiograms by using a 3D-TOF technique, we also performed CE MRA by using a 3D fast field-echo sequence in conjunction with a parallel imaging technique and segmented k-space sampling technique. For the parallel imaging technique, we employed a 5-channel array coil with a time reduction factor of 2.0. As described in detail elsewhere (19), for the segmented k-space sampling technique, we divided the k-space into 6 segments and acquired data from the central part and one of the remaining 5 segments alternately—that is, after collecting the data from the central segment, the data from the remaining 5 segments were collected, starting with the closest one. The accumulated data were then reconstructed as one image. This technique allowed the speed of data collection to be trebled as compared with that in the conventional methods of reconstruction. In all the patients in this series, the scanning was conducted in the coronal plane, by placing a section centered at the postoperative site as visualized in the precontrast MR images. The other imaging parameters were as follows: TR/TE/excitations, 3.1/0.9/1; flip angle, 20°; imaging matrix, 128 × 256; field of view, 26 × 28 cm; partition thickness, 7.5 mm; number of partitions, 10 (section thickness, 75 mm). No interpolation was done in postprocessing. At the start of the scanning, 7 mL of gadolinium was injected via the antecubital vein at the rate of 3 mL/s, followed by 15 mL of saline for flushing, by using a power injector. The postprocessing that involved maximum-intensity projection of the acquired data, obtained after subtracting a set of source images in the early phase from subsequent sets, and gray-scale reversal usually took <15 minutes. For 3D-TOF MRA used in comparison, we performed image reconstruction without employing targeted maximum-intensity projection.

Visual assessment of the CE-MRA images from all of the 17 patients was performed, and the visualized images of the bypass on both the CE-MRA images and 3D-TOF MR angiograms were scored on a 3-point scale as follows: 2 = good; 1 = fair; and 0 = poor. A score of 2 was assigned when the anastomosis and secondary or more distal branches of the recipient vessels connected to the anastomosis or graft artery could be demonstrated. A score of 1 was assigned when the anastomosis and only recipient branches immediately distal to the anastomosis or graft artery could be demonstrated. A score of 0 was assigned when neither the anastomosis nor any of the recipient branches could be visualized. As we assessed both EC and IC postoperative vessels, it was difficult to include a precise control group in this study for comparison. In 6 patients, we also assessed conventional DSA images obtained within one month after the MR study in terms of the visualization of the bypass flow. All the CE-MRA images and MR angiograms were reviewed by 2 radiologists in a blinded fashion to the finally assessed status of the bypass surgery and/or the findings in the conventional DSA images. In cases whose conventional DSA was not available, we used 3D-TOF MR angiograms as the standard determining the conditions of the bypass by comparison with the corresponding EC and IC vessels on the contralateral side. In cases of disagreement in the assessment of any of the angiograms, the final judgment was reached by consensus. Interobserver concordance of the review of the 3 kinds of angiograms between the 2 readers was evaluated by the kappa test.

Results

The CE-MRA and 3D-TOF MR angiographic images were not degraded by patient motion or technical failure in any of the patients and were rated as being of good diagnostic quality. A temporal resolution of 0.8 s/frame was obtained with our CE-MRA technique, which was twice that obtained with the CE-MRA technique employed before the introduction of the parallel imaging technique.

At the initial assessment, the 2 readers' ratings agreed in 16 (94%) patients with a kappa value of 0.77 (substantial reproducibility), in 14 (82%) patients with a kappa value of 0.58 (moderate reproducibility), and in 6 (100%) patients with a kappa value of 1.00 (perfect reproducibility) in the assessment of CE-MRA images, 3D-TOF MR angiograms, and conventional DSA images, respectively.

Of the 16 patients who underwent STA- or ECA-MCA bypass surgery, the patency of the anastomosis was visualized on the CE-MRA images in all the patients, except in one whose surgery had been performed at another institution. His CE MRA demonstrated failure of surgery, which was first suspected on 3D-TOF MR angiograms. In all of the remaining 15 patients who had successful STA- or ECA-MCA bypass surgery, CE MRA demonstrated flow from the parent artery to M2 or more distal branches. In the ratings of these 15 patients, CE MRA was rated better than 3D-TOF MRA in 12 patients, whereas it was rated as being equally efficient in 3 patients. In the former group of 12 patients, CE MRA allowed visualization of the distal M2 branches and their flow dynamics could be compared with that on the contralateral side (Fig 1). In the patient who had VA-PCA bypass surgery, CE MRA provided better visualization of the flow to the bilateral PCAs and even to the distal basilar artery than 3D-TOF MR angiograms. Overall, CE MRA allowed better visualization of the postoperative bypass than 3D-TOF MRA in 13 patients (76%), whereas the 2 methods were equally efficient in 4 patients (24%). The rating of CE MRA corresponded to that of conventional angiography in

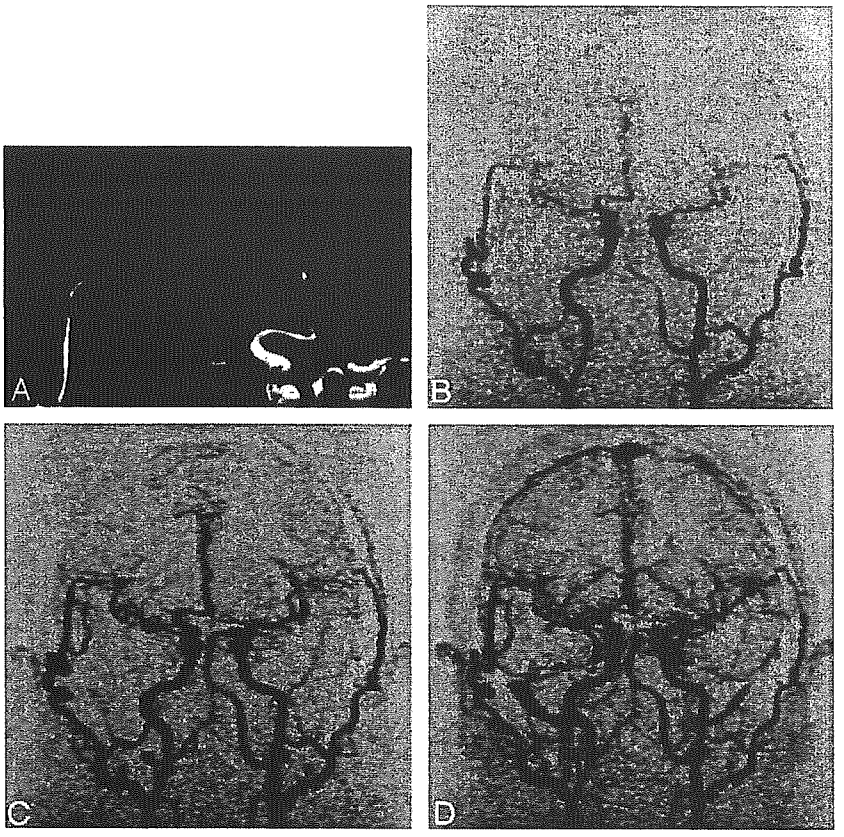

FIG 1. A 57-year-old man 7 months after STA-MCA anastomosis for stenosis of the right MCA.

A, 3D-TOF MR angiogram shows patent anastomosis between the 2 STA branches and distal branches of the right MCA (M2).

B–D, Selected frames of CE MRA show corresponding findings. Flow to the distal parts of the M2 branches is better demonstrated in these images than by MRA.

all of the 6 patients who underwent both the imagings (Fig 2).

Discussion

Postoperative EC-IC bypass is required not only to be patent, but also to provide sufficient blood flow to hypoperfused areas. As stated above, conventional angiography, MRA and CT angiography have been employed in the postoperative assessment of bypass grafts and the distal blood supply. Ultrasonography has also been used for the assessment, both intraoperatively and postoperatively (20, 21). Until now, single-photon emission CT or positron-emission tomography and perfusion study by MR imaging or CT have been considered as the most suitable techniques for the assessment of cerebral blood flow through a bypass graft. It has been believed that MR imaging with diffusion-weighted scanning is of greater value than CT to diagnose early postoperative lesions, including new infarction related to technical failure or homodynamic changes and multifocal hemorrhage with cerebral edema due to normal perfusion pressure breakthrough.

Our results indicated that CE MRA may be at least as useful as 3D-TOF MRA, if not of greater value, for the anatomic evaluation of EC-IC bypasses. Despite the limited number of cases in this study, the findings on CE-MRA images corresponded to those on conventional DSA images in terms of visualization of the branches distal to the anastomosis. These features of CE MRA are considered to be especially advantageous, because the imaging can be performed in combination with MR imaging, including diffusion-weighted imaging, with only the minimal invasiveness associated with the injection of gadolinium.

We consider that our results owe much to technical aspects of our CE-MRA scanning technique. CE MRA can be performed with either 2D or 3D data acquisition. In previous reports, 2D sequences have been employed, with excellent temporal resolution, whereas 3D techniques, which are widely used in time-resolved MRA of other regions of the body, were scarcely employed for the brain, mainly because of the rapid intracranial circulation time. Despite 3D data acquisition, however, we could still achieve a temporal resolution of as good as 0.8 s/frame, by using parallel imaging in combination with the segmented k-space sampling technique. In-plane spatial resolutions for the 2 MR techniques were 2.0 × 1.1 mm for time-resolved, CE MRA and 1.0 × 0.8 mm for 3D-TOF MRA. Although these in-plane sizes of pixels and the partition thickness (5 mm) were not so small, we could still clearly visualize the anastomoses, which are only a few millimeters in diameter, as well as their fine distal branches by our CE MRA. We believe that the maximum-intensity-projection, which effectively increases the signals from vessels containing gadolinium in the postprocessing of the 3D data set in CE MRA, was effective for good visualization of the small arterial branches despite lower spatial resolution when compared with 3D-TOF MRA. In addition,

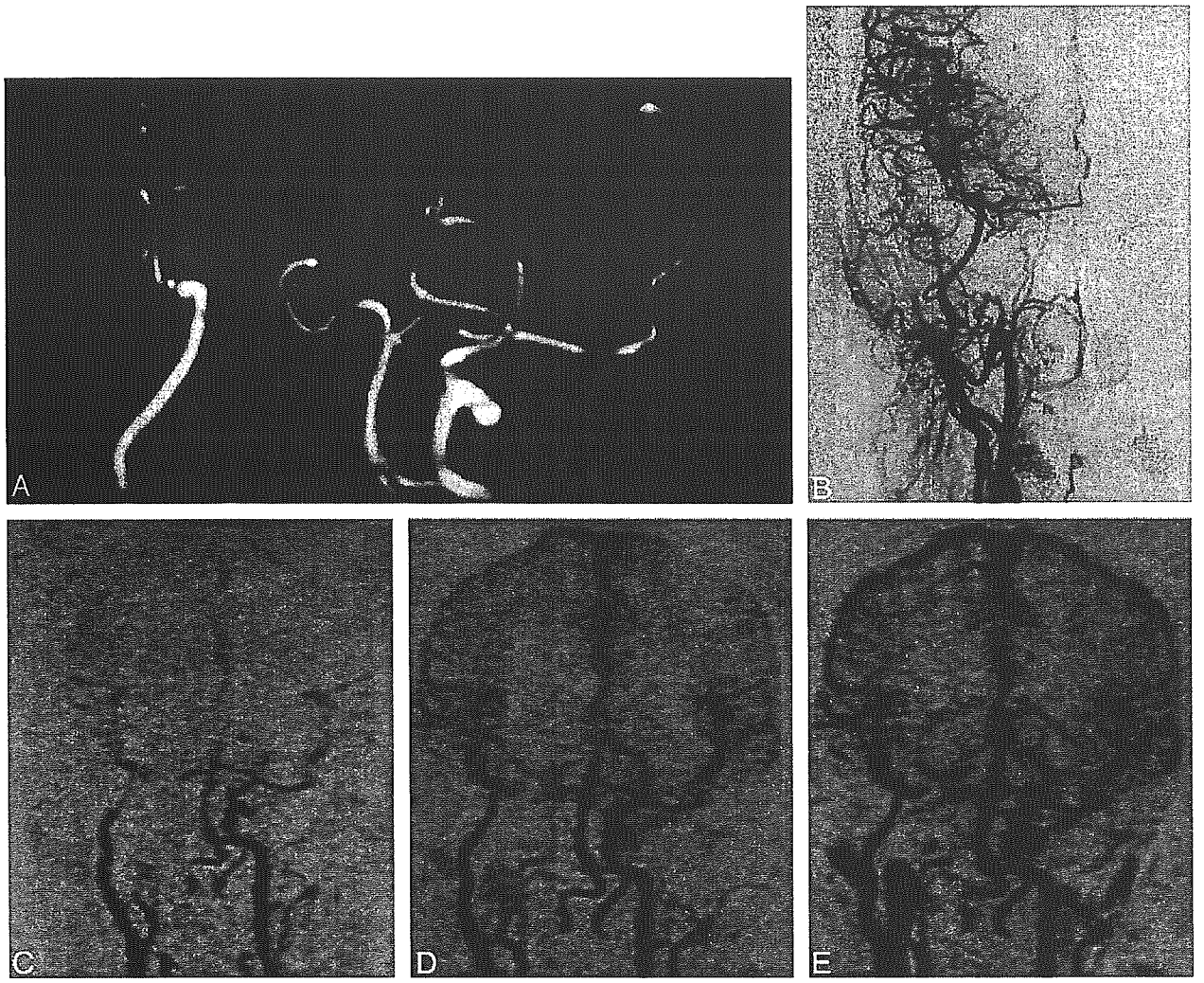

FIG 2. A 43-year-old woman 3 weeks after EC-MCA anastomosis by using a radial-artery graft for occlusion of the right ICA for treatment of a large ICA aneurysm.

A, 3D-TOF MR angiogram shows a patent radial artery graft and distal MCA branches. Note that the more distal MCA branches cannot be fully visualized due to the limited section thickness.

B, Conventional DSA images confirm the patent anastomosis and good distal flow.

C–E, Selected frames of CE MRA show corresponding findings.

we consider that images of multiple phases of CE MRA allowed clear visualization even when the blood flow through a bypass route was rather slow.

The size of the field of view that we selected was the smallest allowed by our hardware and sequence. This resulted in a rather large voxel size, as stated above. The field of view, however, enabled us to visualize long bypasses, such as an EC-MCA anastomosis by using a radial-artery graft, for their entire length (Fig 2). This is another advantage of CE MRA over 3D-TOF MRA, which is generally limited by the section thickness. In addition, with our protocol of injecting 7 mL of gadolinium for a single scan, it is possible to perform CE MRA in an additional plane if indicated. Actually, in 2 patients in this series, we additionally obtained sagittal CE-MRA images, the image quality of which was the same as that of the initial coronal scans. This is probably because, due to subtraction, gadolinium injected for the initial scan does not degrade images of the second scan.

Because our technique provides serial images with good temporal resolution, their pixel-by-pixel analysis, similar to that in perfusion imaging performed by using the dynamic susceptibility contrast technique, may provide quantitative hemodynamic information from the scanned area. This is currently being investigated at our institution.

Conclusion

For postoperative evaluation of EC-IC bypasses, CE MRA can be performed with minimal invasiveness and a short examination time in addition to MR imaging, which can sensitively assess changes in the brain parenchyma. CE MRA by using the parallel imaging technique as well as the segmented k-space

sampling technique is effectively used to assess patency of EC-IC bypasses.

References

1. EC-IC Bypass Study Group. **Failure of extracranial-intracranial arterial bypass to reduce the risk of ischemic stroke: results of an international randomized trial.** *N Engl J Med* 1985;313:1191–1200
2. Yoshimoto Y, Kwak S. **Superficial temporal artery–middle cerebral artery anastomosis for acute cerebral ischemia: the effect of small augmentation of blood flow.** *Acta Neurochir (Wien)* 1995;137:128–137
3. Pikus HJ, Heros RC. **Stroke: indications for emergent surgical intervention.** *Clin Neurosurg* 1999;45:113–127
4. Jack CR Jr, Sundt TM Jr, Fode NC, Gehring DG. **Superficial temporal-middle cerebral artery bypass: clinical pre- and postoperative angiographic correlation.** *J Neurosurg* 1988;69:46–51
5. Okada Y, Shima T, Nishida M, et al. **Effectiveness of superficial temporal artery-middle cerebral artery anastomosis in adult moyamoya disease: cerebral hemodynamics and clinical course in ischemic and hemorrhagic varieties.** *Stroke* 1998;29:625–630
6. Touho H, Karasawa J, Shishido H, et al. **Hemodynamic evaluation before and after the STA-MCA anastomosis, with special reference to measurement of regional transit time with intra-arterial digital subtraction angiography.** *Neurol Med Chir (Tokyo)* 1990;30:663–669
7. Tsuchiya K, Aoki C, Katase S, et al. **Visualization of extracranial-intracranial bypass using multidetector-row helical computed tomography angiography.** *J Comput Assist Tomogr* 2003;27:231–234
8. Wang Y, Johnston DL, Breen JF, et al. **Dynamic MR digital subtraction angiography using contrast enhancement, fast data acquisition, and complex subtraction.** *Magn Reson Med* 1996;36:551–556
9. Tsuchiya K, Katase S, Yoshino A, Hachiya J. **MR digital subtraction angiography of cerebral arteriovenous malformations.** *AJNR Am J Neuroradiol* 2000;21:707–711
10. Aoki S, Yoshikawa T, Hori M, et al. **MR digital subtraction angiography for the assessment of cranial arteriovenous malformations and fistulas.** *AJR Am J Roentgenol* 2000;175:451–453
11. Klisch J, Strecker R, Hennig J, Schumacher M. **Time-resolved projection MRA: clinical application in intracranial vascular malformations.** *Neuroradiology* 2000;42:104–107
12. Wetzel SG, Bilecen D, Lyrer P, et al. **Cerebral dural arteriovenous fistulas: detection by dynamic MR projection angiography.** *AJR Am J Roentgenol* 2000;174:1293–1295
13. Griffiths PD, Hoggard N, Warren DJ, et al. **Brain arteriovenous malformations: assessment with dynamic MR digital subtraction angiography.** *AJNR Am J Neuroradiol* 2000;21:1892–1899
14. Yoshikawa T, Aoki S, Hori M, et al. **Time-resolved two-dimensional thick-slice magnetic resonance digital subtraction angiography in assessing brain tumors.** *Eur Radiol* 2000;10:736–744
15. Tsuchiya K, Aoki C, Katase S, Hachiya J **MR digital subtraction angiography with three-dimensional data acquisition in the diagnosis of brain tumors: preliminary experience.** *Magn Reson Imaging* 2004;22:149–513
16. Pruessmann KP, Weiger M, Scheidegger MB, Boesiger P. **SENSE: sensitivity encoding for fast MRI.** *Magn Reson Med* 1999;42:952–962
17. Wang Y. **Description of parallel imaging in MRI using multiple coils.** *Magn Reson Med* 2000;44:495–499
18. Golay X, Brown SJ, Itoh R, Melhem ER. **Time-resolved contrast-enhanced carotid MR angiography using sensitivity encoding (SENSE).** *AJNR Am J Neuroradiol* 2001;22:1615–1619
19. Naganawa S, Koshikawa T, Fukatsu H, et al. **Contrast-enhanced MR angiography of the carotid artery using 3D time-resolved imaging of contrast kinetics: comparison with real-time fluoroscopic triggered 3D-elliptical centric view ordering.** *Radiat Med* 2001;19:185–192
20. Hyodo A, Mizukami M, Kawase T, et al. **Postoperative evaluation of extracranial-intracranial arterial bypass by means of ultrasonic quantitative flow measurement and computed mapping of the electroencephalogram.** *Neurosurgery* 1984;15:381–386
21. Badie B, Lee FT Jr, Pozniak MA, Strother CM. **Intraoperative sonographic assessment of graft patency during extracranial-intracranial bypass.** *AJNR Am J Neuroradiol* 2000;21:1457–1459

β_2- and β_3-Adrenergic Receptor Polymorphisms Are Related to the Onset of Weight Gain and Blood Pressure Elevation Over 5 Years

Kazuko Masuo, MD, PhD; Tomohiro Katsuya, MD, PhD; Yuxiao Fu, MD; Hiromi Rakugi, MD, PhD; Toshio Ogihara, MD, PhD; Michael L. Tuck, MD

Background—The genes responsible for obesity are candidate genes for obesity-related diseases, such as hypertension. Functional polymorphisms in the β_2- and β_3-adrenergic receptors have been reported to be associated with hypertension and obesity.

Methods and Results—To longitudinally clarify the relevance to alterations in β-adrenergic receptor polymorphisms related to weight gain, blood pressure (BP) elevation, and sympathetic nerve activity as measured by plasma norepinephrine level, we studied 160 young, nonobese, normotensive men. Changes in body weight, BP, plasma norepinephrine levels, and β_2-adrenergic (Arg16Gly, Gln27Glu) and β_3-adrenergic (Trp64Arg) receptor polymorphisms were measured periodically over a 5-year period. Weight gain and BP elevation were defined as $\geq$10% increases from entry levels over 5 years in body mass index or mean BP. The presence of the Gly16 allele of Arg16Gly was associated with a higher frequency of weight gain and BP elevation over the 5-year period. The subjects carrying the Glu27 allele of Gln27Glu and the Trp64 allele of Trp64Arg had a higher frequency of BP elevation. Significantly higher levels of plasma norepinephrine at entry and at year 5 were observed in the subjects with the Gly16 allele of Arg16Gly and the Glu27 allele of Gln27Glu compared with those without the Gly16 or the Glu27 alleles.

Conclusions—These results demonstrate that the Gly16 allele is related to greater weight gain and BP elevation. Additionally, Glu27 and Trp64 alleles are linked to BP elevation. The subjects carrying the β_2-polymorphisms linked to weight gain and BP elevation also have higher plasma norepinephrine levels that are present at entry before weight gain and BP elevation. These findings suggest that β_2-adrenergic receptor polymorphisms in association with a heightened sympathetic nerve activity could predict the future onset of obesity and hypertension, as shown in the 5-year longitudinal study. (***Circulation.*** **2005;111:3429-3434.)**

Key Words: hypertension ■ norepinephrine ■ obesity

Obesity and obesity-related cardiovascular disease are a rapidly growing public health problem,[1] and there is evidence that human obesity and hypertension have strong genetic as well as environmental determinants.[2–4] Reduced energy expenditure and resting metabolic rate are predictive of weight gain, and the sympathetic nervous system participates in regulating energy balance through thermogenesis. The thermogenic effects in obesity have been mainly attributed to the activity of the β_1- and β_2-adrenergic receptors in humans. However, reports of an association of β_2-adrenergic receptor polymorphisms with hypertension and obesity have been discordant.[5–7] Several observations have shown that the Trp64Arg polymorphism of the β_3-adrenergic receptor gene can also be associated with obesity[8–10]; however, this finding has not been confirmed in other studies.[11,12] Few studies have simultaneously taken into account obesity and hypertension as related to polymorphisms of β-adrenoceptor genes in the same study population followed longitudinally for several years. Additionally, plasma norepinephrine levels, as an index of sympathetic nerve activity (SNA), are also included in the present study.

Thus, this study examines the associations of polymorphisms of β-adrenergic receptors with plasma norepinephrine level (index of SNA), weight gain (obesity), and blood pressure (BP) elevation (hypertension) over 5 years in 160 subjects who at entry were young, nonobese, and normotensive.

Methods

Subjects

Subjects were recruited from a cohort of 1121 men who work in a single company in Osaka, Japan, as part of their annual medical

Received November 5, 2004; revision received February 23, 2005; accepted March 4, 2005.

From the Human Neurotransmitter Laboratory, Baker Heart Research Institute, Melbourne, Victoria, Australia (K.M.); Department of Geriatric Medicine, Osaka University Graduate School of Medicine, Suita City, Osaka, Japan (K.M., T.K., Y.F., H.R., T.O.); and Metabolism and Endocrinology Division, Sepulveda VA Medical Center, and David Geffen UCLA School of Medicine, Los Angeles, Calif (M.L.T.).

Correspondence to Kazuko Masuo, MD, PhD, Baker Heart Research Institute, PO Box 6492, St Kilda Rd Central, Melbourne, Victoria 8008, Australia. E-mail kmasuo@baker.edu.au

Circulation **is available at http://www.circulationaha.org** **DOI: 10.1161/CIRCULATIONAHA.104.519652**

TABLE 1. Polymorphism Genotypic Frequencies in Subjects With Significant Weight Gain (≥10%) and Mean BP Elevation (≥10%) Over 5 Years

	Genotypes			χ^2 Test for 3 Genotypes	χ^2 Test for Alleles
Arg16Gly of β_2-adrenoceptor gene	**Arg16/Arg16**	**Arg16/Gly16**	**Gly16/Gly16**		
Frequency					
With weight gain (n=59)	9 (15.3)	33 (55.9)	17 (28.8)	χ^2=7.98, P=0.019	χ^2=6.31, P=0.012
Without weight gain (n=101)	36 (35.6)	46 (45.5)	19 (18.8)		
With BP elevation (n=41)	4 (9.8)	20 (48.8)	17 (41.4)	χ^2=15.43, P<0.001	χ^2=14.42, P<0.001
Without BP elevation (n=119)	41 (34.5)	59 (49.6)	19 (16.0)		
Gln27Glu of β_2-adrenoceptor gene	**Gln27/Gln27**	**Gln27/Glu27**	**Glu27/Glu27**		
Frequency					
With weight gain (n=59)	50 (84.7)	9 (15.3)	0 (0.0)	...	χ^2=2.89, P=0.089
Without weight gain (n=92)	87 (94.6)	5 (5.4)	0 (0.0)		
With BP elevation (n=41)	32 (78.0)	9 (22.0)	0 (0.0)	...	χ^2=8.36, P=0.004
Without BP elevation (n=110)	105 (95.5)	5 (4.5)	0 (0.0)		
Trp64Arg of β_3-adrenoceptor gene	**Trp64/Trp64**	**Trp64/Arg64**	**Arg64/Arg64**		
Frequency					
With weight gain (n=59)	46 (78.0)	11 (18.6)	2 (3.4)	χ^2=7.41, P=0.025	χ^2=2.39, P=0.122
Without weight gain (n=99)	60 (60.6)	38 (38.4)	1 (1.0)		
With BP elevation (n=41)	35 (85.4)	5 (12.2)	1 (2.4)	χ^2=9.16, P=0.010	χ^2=5.25, P=0.022
Without BP elevation (n=117)	71 (60.7)	44 (37.6)	2 (1.7)		

Values in parentheses are percentage of subjects.

evaluation. Subjects at study entry were excluded who were aged >50 years, had obesity (body mass index [BMI] ≥25 kg/m^2),[13,14] had diabetes mellitus (fasting glucose level >100 mg/dL), and had hypertension (≥140/90 mm Hg). We also excluded subjects who were taking medication for hypertension, hyperlipidemia, hyperuricemia, or other illness. Only subjects who had steady body weight (weight had not changed significantly [<5%] over the past year before the entry period) were enrolled in this study.[15,16] After exclusion, 160 young, nonobese (BMI <25 kg/m^2), normotensive (<140/90 mm Hg) men on no medications were enrolled in the present study. Informed consent was obtained from each subject, as approved by the Ethics Committee of Osaka University Graduate School of Medicine, Osaka, Japan.

Measurements

After an overnight fast of >12 hours, BMI, total body fat mass, ratio of waist circumference to hip circumference (waist-to-hip ratio), BP, heart rate, venous sampling for plasma norepinephrine, and extraction of genomic DNA from leukocytes were taken every year for 5 years. BP and heart rate were measured with the subject in the recumbent position with an automated sphygmomanometer (TM-2713, A&D) with an adjusted cuff size, which had been standardized against a mercury sphygmomanometer. The percent body fat mass was determined with impedance measurements (BF-102, Tanita), and total body fat mass (kg) was calculated according to the following formula: (percent body fat mass/100)×body weight (kg).

Laboratory Determinations

Plasma norepinephrine was measured by high-performance liquid chromatography with a fluorometric method as previously described for this laboratory[17] (intra-assay coefficient of variation=2.1%; interassay coefficient of variation=3.6%; sensitivity=0.06 to 120 nmol/L).

Genotyping

Genotyping was performed by the TaqMan assay as previously described.[18] Two polymorphisms in the β_2-adrenergic receptors (arginine/glycine substitution, Arg16Gly; glutamine/glutamate substitution, Gln27Glu) of the β_2-adrenoceptor gene were studied.[6] One polymorphism (tryptophan/arginine substitution, Trp64Arg) of the β_3-adrenoceptor gene was also studied.[19,20] The probes and primers used in the TaqMan assay were as follows. For single-nucleotide polymorphisms in the β_2-adrenergic receptor gene, the probes and primers were as follows: for Arg16Gly, the probes were CGCATGGCTTCCATTGGGTGC and CGCATGGCTTCTATTGGGTGC, and the primers were GGAACGGCAGCGCCTTCT and CAGGACGATGAGAGACATGACGAT; for Gln27Glu, the probes were CTCGTCCCTTTCCTGCGTGACGT and CTCGTCCCTTTGCTGCGTGACGT (the primers used in this assay were the same as those used for Arg16Gly). For the Trp64Arg single-nucleotide polymorphism in the β_3-adrenergic receptors, the probes were TCTCGGAGTCCAGGCGATGGCCA and CTCGGAGTCCGGGCGATGGCC, and the primers were GGAGGCAACCTGCTGGTCAT and CACGAACACGTTGGTCATGGT.

Statistical Analysis

Genotype frequencies and the Hardy-Weinberg equilibrium were estimated with χ^2 test. Values are shown as mean±SD. All data analyses were performed with SPSS 8.0 for Windows programs. Changes in measured parameters within each group and differences among groups were examined by 2-way ANOVA. When these differences were significant, the Dunnett test was used to determine whether the differences of the mean measured variables at entry and 5 years were significant within the groups and among the groups compared from baseline. Values of P<0.05 were considered significant.

Results

Significant weight gain and BP elevation over 5 years were defined as a ≥10% increase in BMI or mean BP compared with values at entry.[16,21] Fifty-nine subjects had significant weight gain over 5 years, and 41 subjects had significant BP elevation. Table 1 shows the prevalence of weight gain and BP elevation at year 5. No subjects with the Glu27/Glu27 polymorphism of the β_2-adrenoceptor were detected in the present study. The allele frequency of Glu27 of the β_2-